Supplementary Information

Surface Circular Photogalvanic Effect in Tl-Pb Monolayer Alloys on Si(111) with Giant Rashba Splitting

Ibuki Taniuchi, Ryota Akiyama, Rei Hobara, and Shuji Hasegawa.*

Department of Physics, The University of Tokyo, Bunkyo, Tokyo 113-0033, Japan

Supplementary note 1. Estimation of the PISHE component

The helicity-dependent photocurrent (HDP) can be induced not only by circular photogalvanic effect (CPGE), but also by photo-induced spin Hall effect (PISHE). PISHE is caused optically by in-plane diffusion of spin current having out-of-plane spin or by out-of-plane diffusion of spin current having in-plane spin, and it is the combination of optical generation of spin current and inverse spin Hall effect[1-3]. Since (Tl, Pb)/Si(111) consists of monolayer Tl-Pb alloy having strong spin-orbit interaction (SOI) and the Si substrate having quite small SOI, PISHE due to spin diffusion in the depth direction is negligible. However, regarding the in-plane diffusion of out-of-plane spin component, HDP by PISHE can be observed when circularly polarized light (CPL) with normal incidence is irradiated at right/left edge of the sample as we reported in the topological insulator Bi_2Se_3 before[1]. If PISHE is observed at a normal incidence of light, the sign of HDP should reverse at the right/left edge. Figure S1 shows the polarization dependence of the photocurrent at the left edge, center, and right edge of the sample in Si(111)-($\sqrt{3}\times\sqrt{3}$)-(Tl, Pb) and Si(111)-(4×4)-(Tl, Pb) by normal-incidence irradiation of the laser λ = 1550 nm. The difference between right-handed CPL and left-handed CPL, corresponding to the parameter *C* in Eq. (1), is almost zero and the sign does not reverse between on the right and left edges. Thus, it is conceivable that PISHE is very small and the origin of HDP observed in this work is most likely due to CPGE.

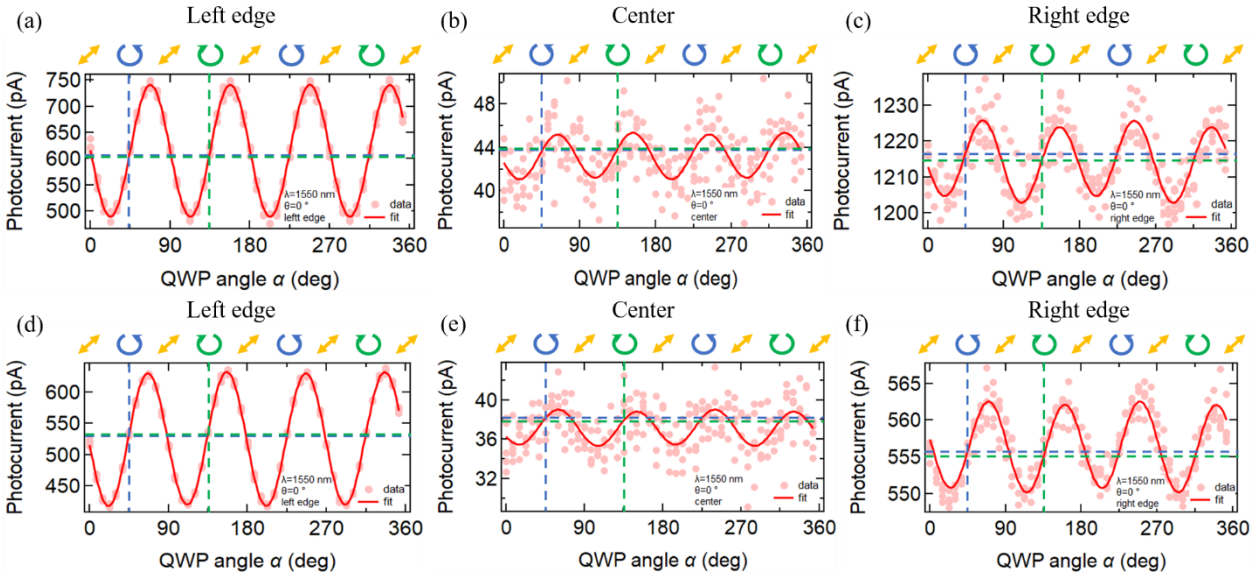

Supplementary Figure 1. Polarization dependence of the photocurrent measured at left edge/center/right edge positions by normal-incidence irradiation of the laser λ = 1550 nm. on the sample in **a,b,c** Si(111)-($\sqrt{3}\times\sqrt{3}$)-(Tl, Pb) and **d,e,f** Si(111)-(4×4)-(Tl, Pb).

Supplementary note 2. Surface structures observed by RHEED

Figure S2 shows reflection high-energy electron diffraction (RHEED) patterns captured in this experiment. The crystal quality is checked *in situ* by RHEED patterns; (a) Si(111)-(7×7), (b) Si(111)-($\sqrt{3}\times\sqrt{3}$)-(Tl, Pb), (c) Si(111)-(4×4)-(Tl, Pb). The flux rates of Tl and Pb at depositions were calibrated using the duration time needed for covering the initial Si(111)-(7×7) to the (1×1) surfaces as shown in (d) 1 ML Si(111)-(1×1)-Tl, and (e) nominal 2-ML-Pb thin film , respectively.

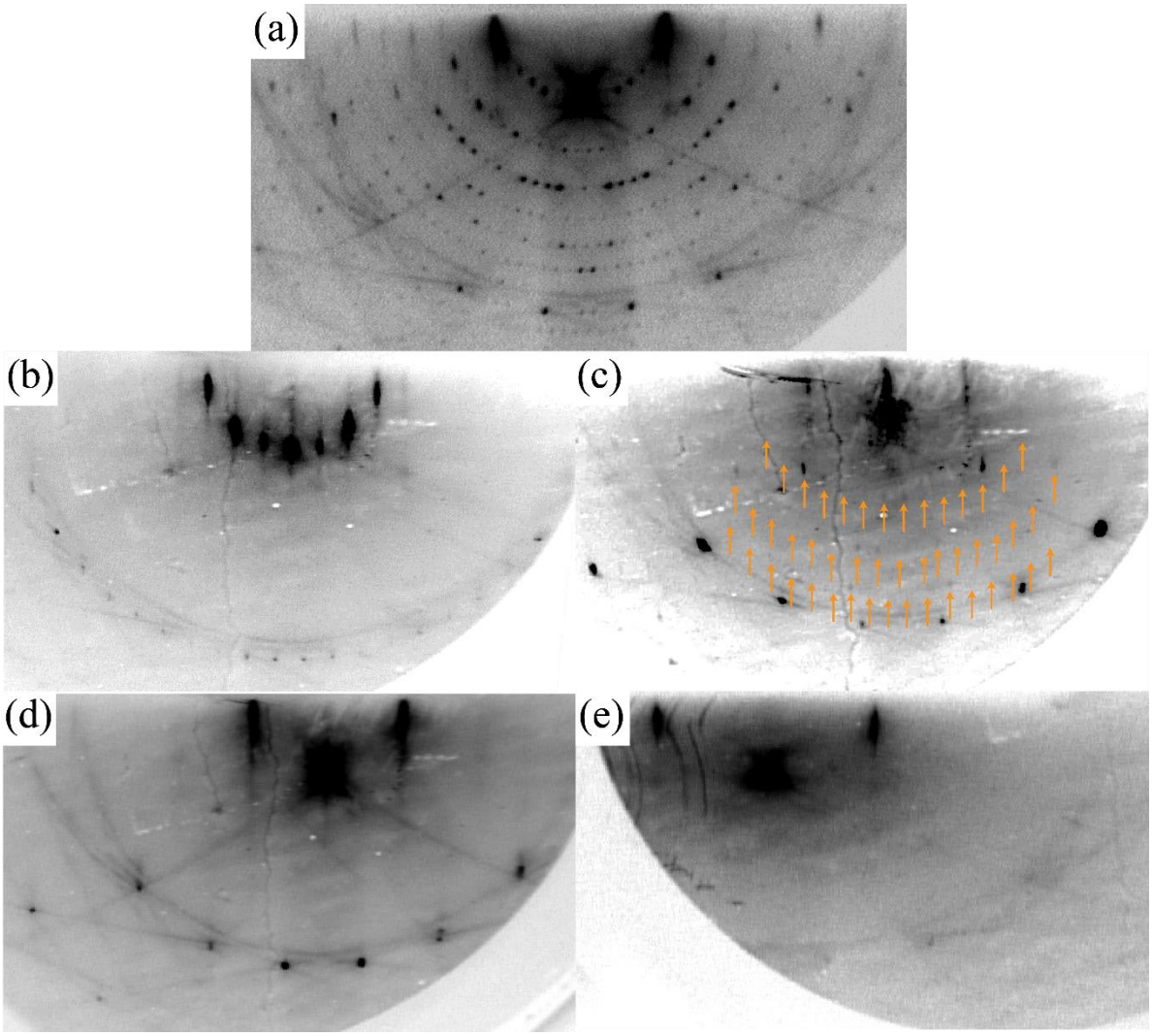

Supplementary Figure 2. RHEED patterns observed with the electron beam of [11$\bar{2}$] incidence on the Si(111) substrate at room temperature in this study. **a** Si(111)-(7×7) **b** Si(111)-(√3×√3)-(Tl, Pb) **c** Si(111)-(4×4)-(Tl, Pb). Representative 4×4 spots of Si(111)-(4×4)-(Tl, Pb) are indicated by orange arrows. **d** 1 ML Si(111)-(1×1)-Tl **e** nominal 2-ML-Pb thin film.

Supplementary note 3. Second-rank pseudo-tensor γ for CPGE

The second-rank pseudo-tensor γ in Eq. (3) represents the symmetry property of materials. In case a material has T symmetry, γ of the material satisfies the following equation,

$$\gamma'_{ab} = T_{ai}T_{bj}|T|\gamma_{ij}. \quad (S1)$$

Here, γ'_{ab} is the pseudo-tensor element after the transformation, T_{xy} is an element of the transforming matrix of T symmetry, $|T|$ is the determinant of the transforming matrix, and γ_{ij} is the

pseudo-tensor element before the transformation. Due to Neumann's principle[4], "the symmetry elements of any physical property of a crystal must include the symmetry elements of the point group of the crystal.", for a system with T symmetry, $\gamma' = \gamma$ should be satisfied. When 3-fold rotation symmetry along z-axis $C_{3(z)}$ and mirror symmetry to xz-plane σ_y are adopted as transformation matrix T, the second-rank pseudo-tensors γ are as follows, respectively;

$$C_{3(z)} = \begin{pmatrix} \cos 120° & -\sin 120° & 0 \\ \sin 120° & \cos 120° & 0 \\ 0 & 0 & 1 \end{pmatrix} : \gamma = \begin{pmatrix} \gamma_{xx} & -\gamma_{yx} & 0 \\ \gamma_{yx} & \gamma_{xx} & 0 \\ 0 & 0 & \gamma_{zz} \end{pmatrix}, \quad (S2)$$

$$\sigma_y = \begin{pmatrix} -1 & 0 & 0 \\ 0 & 1 & 0 \\ 0 & 0 & 1 \end{pmatrix} : \gamma = \begin{pmatrix} 0 & \gamma_{xy} & \gamma_{xz} \\ \gamma_{yx} & 0 & 0 \\ \gamma_{zx} & 0 & 0 \end{pmatrix}. \quad (S3)$$

In this study, x-direction is set along $[11\bar{2}]$ crystal orientation of the Si(111) substrate, y-direction is set along $[\bar{1}10]$ crystal orientation of the Si(111) substrate, and z-direction is set perpendicular to the Si(111) surface (see Fig. 1(e)). Si(111)-($\sqrt{3}\times\sqrt{3}$)-(Tl, Pb) have C_{3v} symmetry[5] and Si(111)-(4×4)-(Tl, Pb) have the most stable structure with C_3 symmetry[6], therefore the respective second-rank pseudo-tensors γ become the following formulas;

$$C_{3v} : \gamma = \begin{pmatrix} 0 & -\gamma_{yx} & 0 \\ \gamma_{yx} & 0 & 0 \\ 0 & 0 & 0 \end{pmatrix}, \quad (S4)$$

$$C_3 : \gamma = \begin{pmatrix} \gamma_{xx} & -\gamma_{yx} & 0 \\ \gamma_{yx} & \gamma_{xx} & 0 \\ 0 & 0 & \gamma_{zz} \end{pmatrix}. \quad (S5)$$

The CPGE current can be described on the macroscopic level by the following phenomenological expression[7];

$$j_\lambda = \sum_\mu \gamma_{\lambda\mu} \hat{e}_\mu E_0^2 P_{circ}. \quad (S6)$$

With the second-rank pseudo-tensor γ of Eqs. (S4) and (S5) and experimental condition of $\hat{\boldsymbol{e}}_y = \mathbf{0}$, CPGE current flows along y-direction and is detected with electrodes clamping the sample at the both ends (see Fig. 1(e)), which is calculated by Eq. (3) (Note: the second-rank pseudo-tensor γ is related to Rashba parameter[8], therefore the second-rank pseudo-tensor γ of Si(111)-($\sqrt{3}\times\sqrt{3}$)-(Tl, Pb) and Si(111)-(4×4)-(Tl, Pb) have different values.).

Supplementary note 4. Dependence of CPGE on the incident angle of light

The dependence of CPGE on the incident angle θ of light is represented by Eq. (4). The curve shape given by Eq. (4) depends on the relative permittivity ε^* of materials. Considering the Fresnel equations and Snell's law at the boundary between material and vacuum, the projection of a unit vector of the light on the x-axis which propagates to x-direction inside of the materials is expressed by the following equation[9];

$$\hat{e}_x = t_p t_s \sin\theta' \,, \tag{S7}$$

where

$$t_p = \frac{2\cos\theta}{\sqrt{\varepsilon^*}\cos\theta + \cos\theta'}, \tag{S8}$$

$$t_s = \frac{2\cos\theta}{\cos\theta + \sqrt{\varepsilon^*}\cos\theta'}, \tag{S9}$$

$$\sin\theta' = \sin\theta/\sqrt{\varepsilon^*}\,. \tag{S10}$$

Here, t_p is the transmission coefficient of the *p*-polarized light, t_s is the transmission coefficient of the *s*-polarized light, θ is the incident angle in the vacuum side, θ' is the angle of refraction in the material side, and ε^* is the relative permittivity of the material.

Supplementary Figure 3 shows curves given by Eq. (4) with various values of relative permittivity ε^*. The maximum and minimum positions depend on the relative permittivity ε^*. When $\varepsilon^* = 1$, maximum (minimum) is achieved at $\theta = 90°$ ($\theta = -90°$). When ε^* increases, the maximum (minimum) position shifts to a smaller (larger) angle θ, finally asymptotic to $\theta = 45°$ ($\theta = -45°$). Even if $\varepsilon^* = 2$, the maximum (minimum) position is $\theta \approx 45°$. Therefore, the parameter *C* of Si(111)-($\sqrt{3} \times \sqrt{3}$)-(Tl, Pb) and Si(111)-(4×4)-(Tl, Pb) in Fig. 3(a) is significantly enhanced with increasing θ up to 60° because of $\varepsilon^* \sim 1.0$ - 1.1, indicating a negligible absorption of the light with the negligibly small effect of refraction.

In the refraction and transmission processes of Fresnel equations and Snell's law, the dielectric constant ε^* represents how much transmission occurs and how much light is bent by refraction. In other words, the dielectric constant ε^* determines attenuation coefficients t_p, t_s, and angle of refraction θ' (namely reflection coefficient). In the vacuum side $\varepsilon^* = 1.0$ whereas in the bulk side (Si substrate) $\varepsilon^* = 11.9$. Naturally, the value of ε^* in the vacuum and the bulk should be smoothly connected to each other at the Si surface. Therefore, ε^* of ~ 1.0 in the vacuum increases up to 11.9 with going deep into the bulk. The gradient of ε^* in the direction of depth depends on the magnitude of ε^* of the material, which in the case of Si varies with a width of about 4 nm[10-12]. Therefore, it is estimated that ε^* near the surface of the monolayer superstructure is almost equal to $\varepsilon^* = 1.0$. In this way, such an effect of reduced dielectric constant near the vacuum interface is more pronounced when the film thickness is thin, which is known to be a problem, for example, when one wants to ensure capacitance in thin-film devices[13-16].

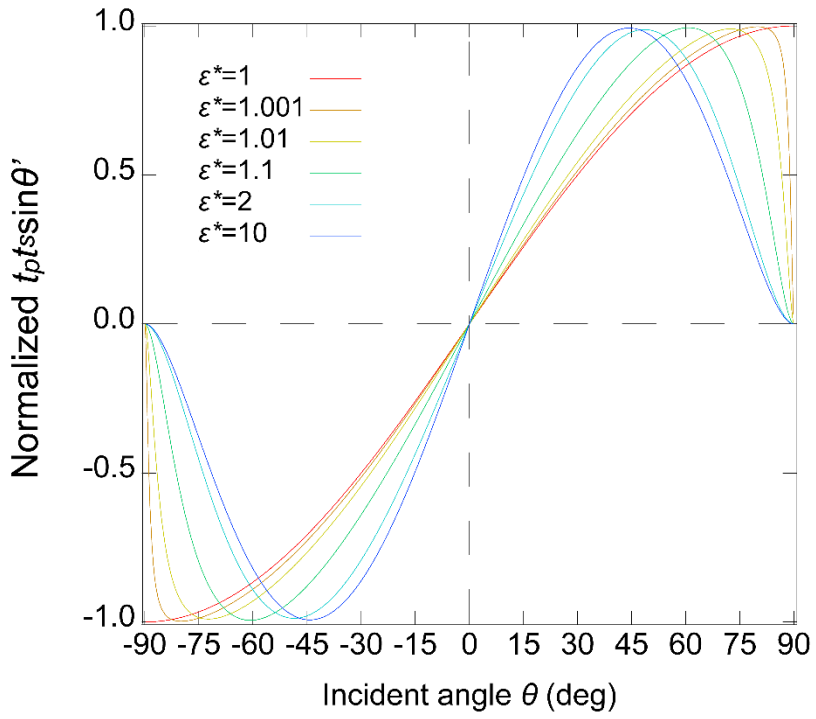

Supplementary Figure 3. Angle of light incidence dependences of $t_p t_s \sin\theta'$ in various values of relative permittivity ε^*. $t_p t_s \sin\theta'$ is normalized for comparison with the peak value; with larger ε^*, the peak becomes smaller.

Supplementary note 5. Photocurrent with λ = 635 nm laser light

A visible red laser with λ = 635 nm is also irradiated on the samples and CPGE is measured (Fig. S4). The 180° periodicities are not observed, that is, CPGE is not observed. This is reasonable because the laser with λ = 635 nm (1.95 eV) excites carriers in the Si substrate over the band gap (1.1 eV) to produce photocurrent in nA range and hides the surface response, that is, CPGE.

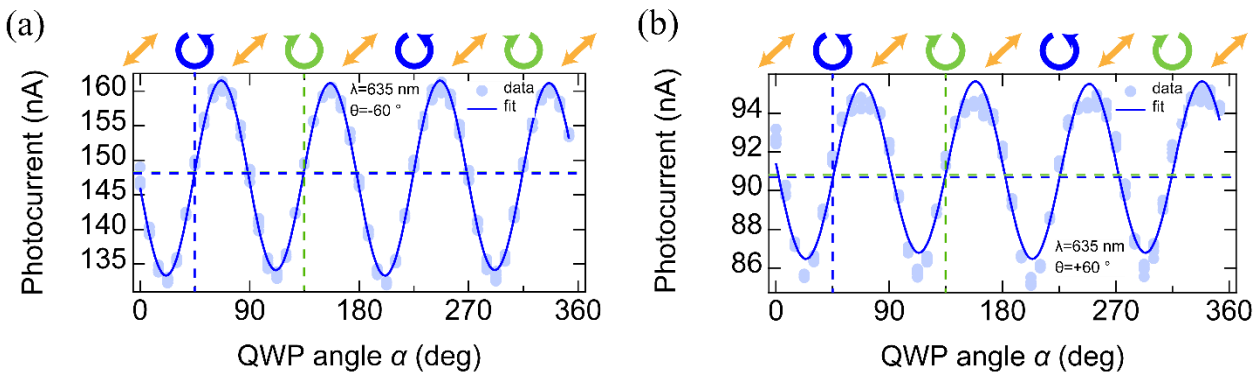

Supplementary Figure 4. Polarization dependence of the photocurrent measured on Si(111)-($\sqrt{3}\times\sqrt{3}$)-(Tl, Pb) with λ = 635 nm. at the angle of incidence **a** θ = - 60° and **b** θ = + 60°, respectively. The photocurrent has almost the same value between right- and left-handed CPL.

Supplementary note 6. The band structures of (Tl, Pb)/Si(111) and optical transition

In this work, the band structures play important roles in optical transitions with red and near infra-red (NIR) light. Since Si single crystal is an indirect transition semiconductor having indirect bulk band gap (E_g = 1.1 eV), the laser with λ = 635 nm (1.95 eV) excites not only carriers in (Tl, Pb) surface layer but also carriers in the Si substrate over the band gap (1.1 eV) to produce photocurrent in nA range (Fig. S4).

On the other hand, the critical points having large joint density of states (JDOS) in the Brillouin zone, which are related to the optical transitions with NIR (~ 0.8 eV) light, can be found in surface Rashba-splitting band dispersions around $\bar{M}$, $\bar{\Gamma}$, and $\bar{K}$ in the case of Si(111)-($\sqrt{3}\times\sqrt{3}$)-(Tl, Pb) as shown in Fig. S5(a)[17]. However, we can exclude transitions around $\bar{\Gamma}$ point because the energy gap around $\bar{\Gamma}$ point is too large for the incident photon energy. In the case of Si(111)-(4×4)-(Tl, Pb) as shown in Fig. S5(b)[6], there are many critical points having large JDOS other than $\bar{M}$, $\bar{\Gamma}$, and $\bar{K}$, so we cannot narrow down the excitation paths.

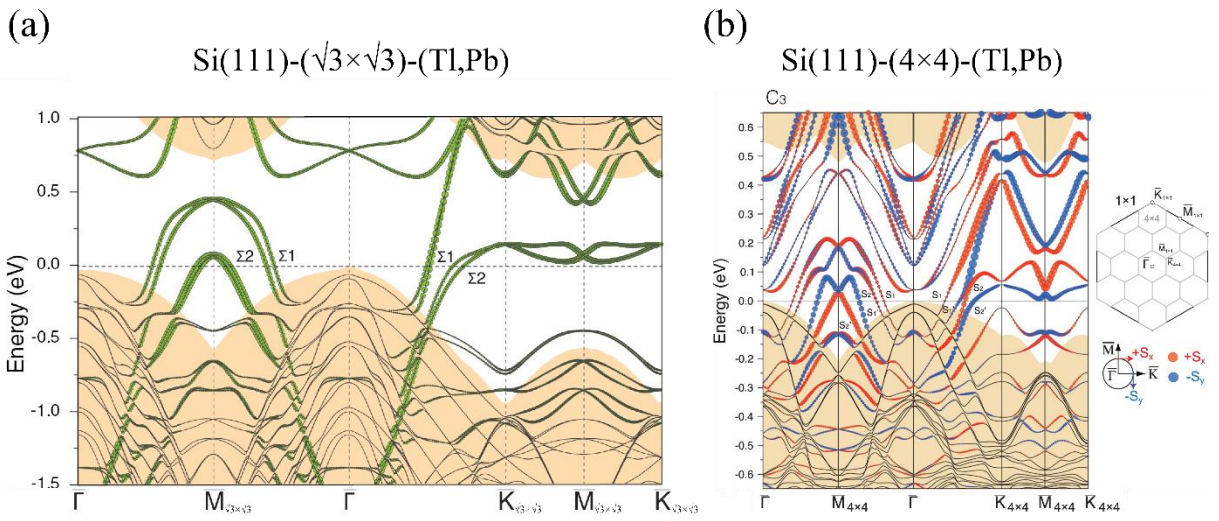

Supplementary Figure 5. The whole band structures of **a** Si(111)-($\sqrt{3}\times\sqrt{3}$)-(Tl, Pb) and **b** Si(111)-(4×4)-(Tl, Pb). The band dispersion figures are cited from [6,17]. Green markers in **a** and red and blue markers in **b** indicate the surface Rashba-split bands. **a** is reprinted and modified from [17], Copyright (2017), with permission from IOP Publishing Ltd.. **b** is reprinted and modified from [6], Copyright (2017), with permission from Elsevier.

Supplementary note 7. Calibration of center position with invisible light λ = 1550 nm

Since NIR light cannot be seen directly, one way to decide whether the laser illuminates the sample or not is by measuring the photocurrent. When the laser is irradiated outside the sample, no photocurrent is generated, and when the laser spot is subsequently moved toward the center of the sample, the sample edge is recognized by that the photocurrent begins to be generated. So, we can judge the position which the laser spot illuminates on the sample. When we measured the *x*(horizontal)-direction dependence of the photocurrent (see Fig. 1(e)), we started to measure the photocurrent at the left edge of the sample, and moved the laser spot position toward the right edge by a certain distance step by step and measure the photocurrent repeatedly, until the spot reached the right edge. Then, we estimated the shift distance by the number of repeats and the sample width, which enables us to determine the center position of the sample. This process was done at each incident angle of the light θ (Fig. S6).

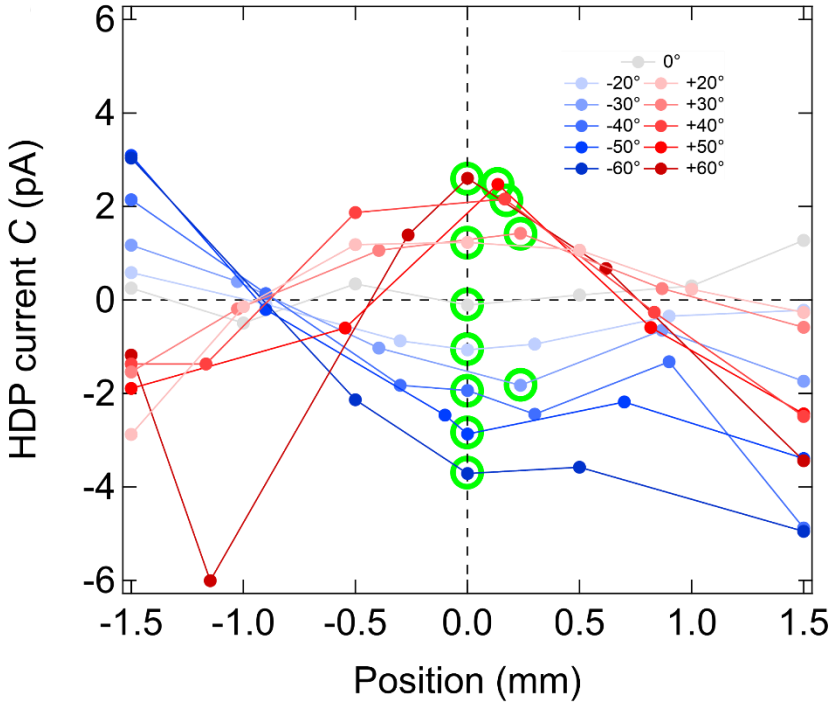

Supplementary Figure 6. Laser-spot position dependence of the HDP current *C* measured along *x* direction on Si(111)-($\sqrt{3}\times\sqrt{3}$)-(Tl, Pb) with λ = 1550 nm at various incident angles θ from - 60° to + 60°. The data surrounded by green circles are adopted as the center position data.

Supplementary note 8. Confirmation of displacement effect of laser spot

Regarding the position-related effects of the laser concerning QWP rotation, these often confuse and can mislead us, so we must be careful. In this study, we have confirmed before the measurement whether we can exclude them or not as follows:

If the position-related effects by the QWP angle occur, it often results from the misalignment of the optical axis of QWP (Fig. S7(a)), which makes laser spot rotate around an optical axis with rotating the QWP (Fig. S7(b)). If this rotation occurs, unintentional photocurrent dependence on QWP angle α which has a periodicity of 360° should be seen when the laser spot illuminates at the sample edge. This is because the rotating spot gets out of the edge in a certain angle range as shown in Fig. S7(c) and the photocurrent is written by, instead of Eq. (1),

$$J = C\sin 2(\alpha+\alpha_0) + L_1\sin 4(\alpha+\alpha_0) + L_2\cos 4(\alpha+\alpha_0) + N_{displace}\sin(\alpha+\beta+\alpha_0) + D. \quad (S11).$$

Here, $N_{displace}$ reflects the magnitude of the displacement and β is the phase shift term. The 4th term in Eq. $(S11)$ means that J changes with 360° cycle by the QWP rotation. The observed data and the fitting result by Eq. (R1) are shown in Fig. S7 (d), and $N_{displace}$ = 3.15 ± 0.68, D = 615 ± 0.48, so the ratio of $N_{displace}/D$ = 3.15/615 = 0.51 %. This tiny ratio indicates that the spot displacement effect due to the QWP misalignment is negligibly small, at least an order of magnitude smaller

than the radius. The reason for this is that if the displacement is larger than the spot radius, the ratio should be 100 % at the sample edge because half of the spot area generates the half photocurrent at $\alpha+\beta = 0°$ and $\alpha+\beta = 180°$, full of the spot area generates the full photocurrent at $\alpha+\beta = 90°$, and the spot does not illuminate the sample at all $\alpha+\beta = 270°$. In this situation, $N_{displace}$ and D are comparable as shown in Fig. S7 (c) (lower figure). However, in our experiments, such a change in the photocurrent with 360° periodicity cannot be seen as in the graph of Fig. S7 (d), that is, the spot-position-related effect due to the QWP misalignment is small enough to ignore.

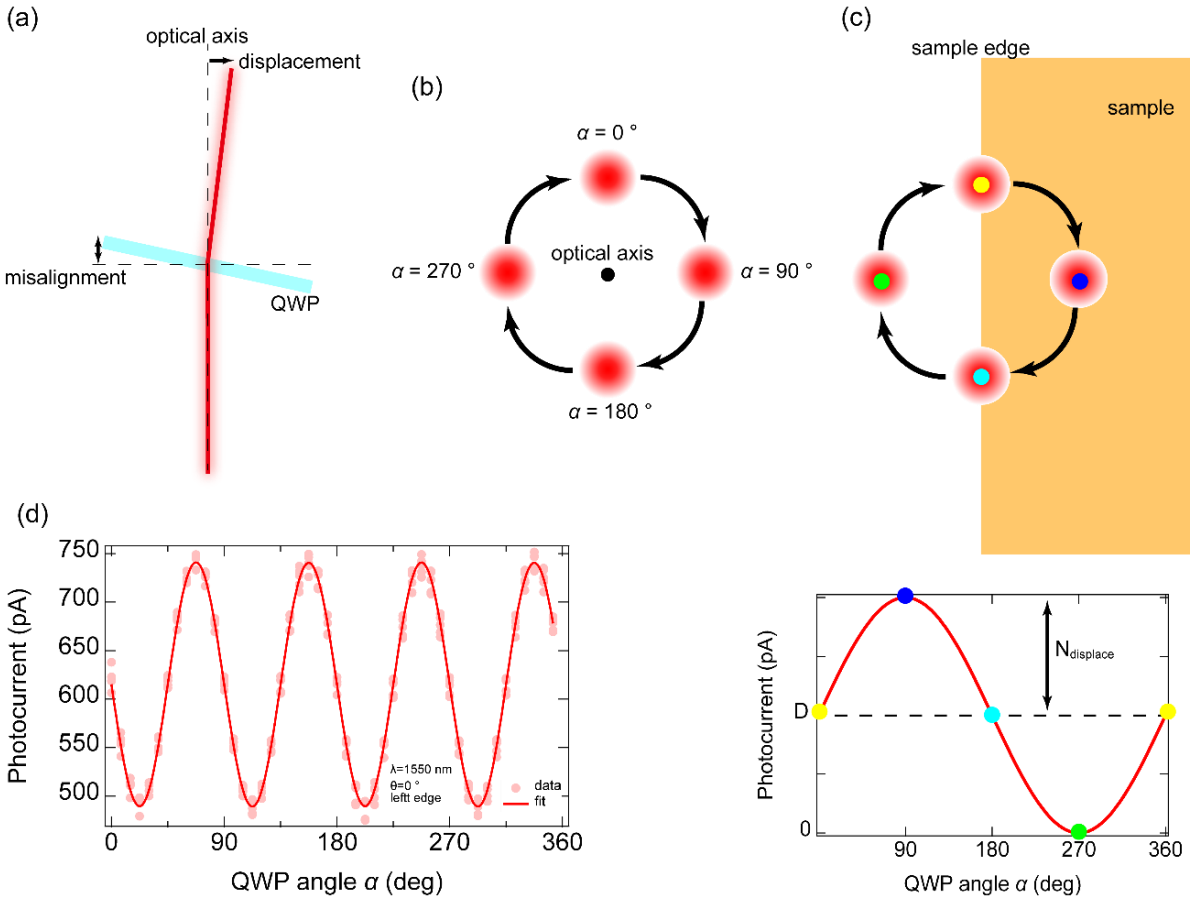

Supplementary Figure 7. Images of displacement effect. Schematics of **a** a spot displacement due to misalignment of QWP, **b** a spot rotation by the misalignment when the QWP rotates in $\beta = 0$ condition of Eq.$(S11)$, and **c** a situation when the laser light illuminates the sample edge with misalignment in $\beta = 0$ condition. The lower figure is a schematic showing the QWP angle dependence of the photocurrent component with the displacement effect. The color points correspond to the spot position in the upper figure. **d** Polarization dependence of the photocurrent measured on the left edge in the samples of Si(111)-($\sqrt{3}\times\sqrt{3}$)-(Tl, Pb) with $\lambda = 1550$ nm with the incidence light of $\theta = 0°$.

Supplementary References

1. Fan, D., Hobara, R., Akiyama, R. & Hasegawa, S. Inverse spin Hall effect induced by asymmetric illumination of light in topological insulator Bi_2Se_3. Phys. Rev. Research **2**, 023055 (2020).

2. Hirai, Y., Yoshikawa, N., Hirose, H., Kawaguchi, M., Hayashi, M. & Shimano, R. Terahertz Emission from Bismuth Thin Films Induced by Excitation with Circularly Polarized Light. Phys. Rev. Applied **14**, 064015 (2020).

3. Yu, J., Zeng, X., Zhang, L., He, K., Cheng, S., Lai, Y., Huang, W., Chen, Y., Yin, C. & Xue, Q. Faraday Rotation Due to Surface States in the Topological Insulator $(Bi_{1-x}Sb_x)_2Te_3$. Nano Lett. **17**, 12, 7878–7885 (2017).

4. Neumann, F. E. *Vorlesungen über die Theorie der Elastizität der festen Körper und des Lichtäthers*, B.G.Teubner-Verlag, Leipzig, (1885).

5. Matetskiy, A. V., Ichinokura, S., Bondarenko, L. V., Tupchaya, A. Y., Gruznev, D. V., Zotov, A. V., Saranin, A. A., Hobara, R., Takayama, A. & Hasegawa, S. Two-Dimensional Superconductor with a Giant Rashba Effect: One-Atom-Layer Tl-Pb Compound on Si(111). Phys. Rev. Lett. **115**, 147003 (2015).

6. Mihalyuk, A.N., Hsing, C.R., Wei, C.M., Gruznev, D.V., Bondarenko, L.V., Tupchaya, L.V., Zotov, A.V. & Saranin, A.A. One-atom-layer 4×4 compound in (Tl, Pb)/Si(111) system. Surf. Sci. **657**, 63-68, (2017).

7. Ivchenko, E. L. & Pikus, G. E. *Superlattices and Other Heterostructures. Symmetry and Optical Phenomena*, Springer, 1997

8. Giglberger, S., Golub, L. E., Bel'kov, V. V., Danilov, S. N., Schuh, D., Gerl, C., Rohlfing, F., Stahl, J., Wegscheider, W., Weiss, D., Prettl, W. & Ganichev, S. D. Rashba and Dresselhaus spin splittings in semiconductor quantum wells measured by spin photocurrents. Phys. Rev. B **75**, 035327 (2007).

9. Ganichev, S. D. & Prettl, W. Spin photocurrents in quantum wells. J. Phys. Condens. Matter **15**, R935–R983 (2003).

10. Yoo, H. G. & Fauchet, P. M. Dielectric constant reduction in silicon nanostructures. Phys. Rev. B **77**, 115355 (2008).

11. Markov, S., Penazzi, G., Kwok, Y., Pecchia, A., Aradi, B., Frauenheim, T. & Chen, G. Permittivity of Oxidized Ultra-Thin Silicon Films From Atomistic Simulations. IEEE Electron

Device Lett. **36**, 10, 1076-1078, (2015).

12. Giustino, F. & Pasquarello, A. Theory of atomic-scale dielectric permittivity at insulator interfaces. Phys. Rev. B **71**, 144104 (2005)

13. Hwang, C. S. Thickness-dependent dielectric constants of (Ba,Sr)TiO_3 thin films with Pt or conducting oxide electrodes. J. Appl. Phys. **92**, 432 (2002).
14. C. Zhou and D. M. Newns, J. Appl. Phys. **82**, 3081 (1997).

15. Padmini, P., Taylor, T. R., Lefevre, M. J., Nagra, A. S., York, R. A. & Speck, J. S. Realization of high tunability barium strontium titanate thin films by rf magnetron sputtering. Appl. Phys. Lett. **75**, 3186 (1999).

16. Osada, M. & Sasaki, T. The rise of 2D dielectrics/ferroelectrics. APL Mater. **7**, 120902 (2019).

17. Gruznev, D. V., Bondarenko, L. V., Tupchaya, A. Y., Eremeev, S. V., Mihalyuk, A. N., Chou, J. P., Wei, C. M., Zotov, A. V. & Saranin, A. A. 2D Tl–Pb compounds on Ge(111) surface: atomic arrangement and electronic band structure. J. Phys.: Condens. Matter **29** 035001 (2017)